

Synergetic Use of the WSR-88D Radars, GOES-R Satellites, and Lightning Networks to Study Microphysical Characteristics of Hurricanes

JIAXI HU

*Cooperative Institute for Mesoscale Meteorological Studies, University of Oklahoma, and
NOAA/OAR, National Severe Storms Laboratory, Norman, Oklahoma*

DANIEL ROSENFELD

Department of Atmospheric Sciences, Hebrew University of Jerusalem, Jerusalem, Israel

ALEXANDER RYZHKOV AND PENGFEI ZHANG

*Cooperative Institute for Mesoscale Meteorological Studies, University of Oklahoma, and
NOAA/OAR, National Severe Storms Laboratory, Norman, Oklahoma*

(Manuscript received 22 May 2019, in final form 16 April 2020)

ABSTRACT

This study analyzes the microphysics and precipitation pattern of Hurricanes Harvey (2017) and Florence (2018) in both the eyewall and outer rainband regions. From the retrievals by a satellite red–green–blue scheme, the outer rainbands show a strong convective structure while the inner eyewall has less convective vigor (i.e., weaker upper-level reflectivities and electrification), which may be related to stronger vertical wind shear that hinders fast vertical motions. The WSR-88D column-vertical profiles further confirm that the outer rainband clouds have strong vertical motion and large ice-phase hydrometeor formation aloft, which correlates well with 3D Lightning Mapping Array source counts in height and time. From the results from this study, it is determined that the inner eyewall region is dominated by warm rain, whereas the external rainband region contains intense mixed-phase precipitation. External rainbands are defined here as those that reside outside of the main hurricane circulation, associated with surface tropical storm wind speeds. The synergy of satellite and radar dual-polarization parameters is instrumental in distinguishing between the key microphysical features of intense convective rainbands and the warm-rain-dominated eyewall regions within the hurricanes. Substantial amounts of ice aloft and intense updrafts in the external rainbands are indicative of heavy surface precipitation, which can have important implications for severe weather warnings and quantitative precipitation forecasts. The novel part of this study is to combine ground-based radar measurement with satellite observations to study hurricane microphysical structure from surface to cloud top so as to fill in the gaps between the two observational techniques.

1. Introduction

From 1851 to 2017, 292 hurricanes directly hit the mainland U.S. coastline, and 91 of them are categorized as major hurricanes (NOAA 2018). Landfalling hurricanes bring high winds, storm surge, flooding, and tornadoes, which make them one of the costliest natural disasters on Earth in terms of human lives and property

loss. The severity of hurricanes often refers to their maximum wind speed (Iacovelli 1999). Yet the major casualty and property loss associated with hurricanes are mainly caused by heavy precipitation and flooding, which are weakly related to the wind speeds (Czajkowski and Done 2014).

Hurricane Harvey started as a weak tropical storm and intensified into a category 4 hurricane before landing near Corpus Christi, Texas, on 25 August 2017. Harvey stalled at southeast Texas for 5 days and produced more than 60 in. (1.52 m) of precipitation within the Houston metropolitan area. At least 68 direct fatalities have been confirmed, 36 of which were in the Houston urban area and were attributed to floods

Supplemental information related to this paper is available at the Journals Online website: <https://doi.org/10.1175/JAMC-D-19-0122.s1>.

Corresponding author: Jiaxi Hu, jiaxi.hu@noaa.gov

DOI: 10.1175/JAMC-D-19-0122.1

© 2020 American Meteorological Society. For information regarding reuse of this content and general copyright information, consult the AMS Copyright Policy (www.ametsoc.org/PUBSReuseLicenses).

(Blake and Zelinsky 2018). The total estimated cost of Harvey is \$125 billion, and it ranks number 2 after Hurricane Katrina (2005) among the most expensive hurricanes in U.S. history (Blake and Zelinsky 2018). Hurricane Florence was only category 1 when it landed near Wrightsville Beach, North Carolina, on 14 September 2018. However, Florence is the ninth costliest hurricane in the U.S. history (\$22 billion) because of its heavy precipitation (Stewart and Berg 2019). Florence dumped more than 30 in. (0.76 m) over the coastal area of North Carolina. The direct death count due to Florence is 22, and at least 17 victims were killed by freshwater flooding (Stewart and Berg 2019).

In search of the mechanisms causing these floods, previous observational studies of the precipitation and microphysical structures of tropical cyclones (TCs) utilized mainly single-polarization radars (Chen et al. 2012; Tokay et al. 2008; Ulbrich and Lee 2002; Wilson and Pollock 1974) and dual-polarization radars (Brown et al. 2016; Chang et al. 2009; Didlake and Kumjian 2017, 2018; Feng and Bell 2019; May et al. 2008; Wang et al. 2016; Yu and Tsai 2013). As compared with the traditional single-polarization radars, the dual-polarization radars can provide information about hydrometeor number concentrations, size, shape, orientation, and dielectric properties within each radar volume scan. These features can be used to distinguish between liquid- and ice-phase hydrometeors under different microphysical and dynamical processes (Kumjian and Ryzhkov 2012; Ryzhkov and Zrnić 2019).

Satellite remote sensing techniques have also been applied in an effort to improve understanding of the mechanisms that control TCs genesis and intensification (Tourville et al. 2015; Wu and Soden 2017). The *Geostationary Operational Environmental Satellite-16 (GOES-16)* provides data via 16 Advanced Baseline Imager (ABI) channels with spatial resolution from 500 m to 2 km and temporal resolution from 30 s to 15 min over much of the continental United States. The Geostationary Lightning Mapper (GLM) on *GOES-16* is the first operational lightning mapper in a geostationary orbit. The flash data can be used as a good indicator of convection intensity (Ávila et al. 2010; Rasmussen et al. 2014; Xu et al. 2017). Previous remote sensing efforts (Dai et al. 2007; Goren and Rosenfeld 2012; Lensky and Rosenfeld 2008; Rosenfeld 2018; Rosenfeld and Lensky 1998; Rosenfeld et al. 2012, 2014; Zheng and Rosenfeld 2015; Zhu et al. 2014) have shown great potential for the study of TCs' microphysical structure by using polar-orbiting satellite data. These methods can be applied using *GOES-16*, providing insight into microphysical properties and time evolution of

hurricane systems, similar to the Weather Surveillance Radar-1988 Doppler (WSR-88D) network.

Surface precipitation is strongly influenced by the microphysical processes in the upper parts of the storms (Chang et al. 2015). This study will focus on using a combination of satellite and radar observations for better understanding of TC microphysical structure and precipitation formation. The observational data and analysis methods are described in section 2. A detailed analysis of the inner and external rainbands in Hurricanes Harvey and Florence by using both radar and satellite observations is presented in section 3. A conceptual model is suggested in section 4. A summary and conclusions are given in section 5.

2. Methods

a. Satellite data and processing

1) GOES-16 CONVECTIVE RGB SCHEME

Inherited from the previous Rosenfeld–Lensky technique (Rosenfeld and Lensky 1998; Rosenfeld et al. 2008), the new *GOES-16* version of the convective red–green–blue (RGB) displays reflectance (%) in the solar channels and brightness temperature (BT; K) in the thermal channels.

Information on the RGB channels is given in Table 1. The 0.86- μm reflectance ($r_{0.86}$), in red, approximates the cloud optical depth and the amount of vertically integrated cloud water and ice (Lensky and Rosenfeld 2008), since radiation in the 0.86- μm channel is much less absorbed by cloud droplets when compared with IR bands. The 1.6- μm reflectance ($r_{1.6}$), in green, is larger for smaller cloud-top ice crystal size. The 10.4- μm BT (T10.4) modulates the blue that refers to the cloud-top brightness temperature. All RGB channels are for the dynamic range from 0.1 to 99.9 percentiles to exclude outliers. For the green channel, the color percentile calculation is based on pixels with 10.4- μm BT less than 233.15 K (homogenous ice nucleation temperature) to focus on icy cloud tops.

Different gamma settings were applied to allow certain features to stand out: $\Gamma < 1$ stretches the colors of the larger values at the expense of the low values, whereas $\Gamma > 1$ does the opposite. For red and green, $\Gamma = 0.5$ enhances the cloud pixels with deeper cloud optical depth ($r_{0.86}$) and cloud top with higher concentration of small ice crystals ($r_{1.6}$). For the blue beam, $\Gamma = 1.5$ delineates the colder and taller cloud-top pixels (T10.4).

This color scheme is useful for convective cloud identification. In this color scheme, the ocean appears blue (point A in Fig. 1a) because the sea surface is relatively warm, with only high T10.4 depicted. Cirrocumulus

TABLE 1. Layout of the convective RGB scheme (Lensky and Rosenfeld 2008). The scheme’s channel information, stretch values, and percentile ranges are provided.

	<i>GOES-16</i> quantity	Stretch	Percentile
Red	r0.86	$\Gamma = 0.5$	0.1–99.9
Green	r1.6	$\Gamma = 0.5$	0.1–99.9
Blue	T10.4	$\Gamma = 1.5$	(10.4- μm BT < 233.15 K) 0.1–99.9

clouds (point B in Fig. 1a) appear greenish because they are optically thin (low red; r0.86), with cold cloud top (relatively low blue; T10.4) and small ice crystals (high green; r1.6). Convective cores (point C in Fig. 1a) have extremely cold cloud tops (very low blue; T10.4), high cloud optical depth (high red; r0.86), and a large number of small ice crystals (high green; r1.6), which make them appear yellow. Point E (Fig. 1a) shows the nonconvective clouds (purple) with warm cloud tops (high blue; T10.4), a large amount of vertically integrated cloud water (high red; r0.86), and almost no ice at cloud top (low green; r1.6). The nonconvective cores (point D in Fig. 1a; Harvey eyewall) have features similar to the external convective band (point C in Fig. 1a) in all three bands; however, the convective band exhibits greater cloud-top roughness, as shown by the spatial variability of the texture or its boiling appearance. The roughness of each 2D *GOES-16* snapshot pixel is shown by the standard deviation of the surrounding 3-by-3 r1.6 pixels (Gademawla et al. 2002). The cloud edge pixels are ignored for the roughness calculation. Comparison

of C and D regions shows an obvious difference in cloud-top roughness (Fig. 1b). Clouds with deep vertical development share the same features of large water content, cold cloud top, and a high concentration of small ice crystals, but the enhanced roughness at the cloud top indicates stronger vertical motions.

2) *GOES-16* GLM DATA

The GLM on *GOES-16* uses a single-channel (777.4 nm) near-infrared optical transient detector for optical scene change detection every 2 ms. The GLM data spatial resolution is about 10 km with 90% flash detection efficiency and a 20-s product latency (Rudlosky et al. 2019).

In this study, the 15-min full-disk *GOES-16* GLM data are used to examine Harvey’s and Florence’s cloud-top convective features. The GLM ± 7.5 min of data were overlaid on each RGB image. The GLM parameters such as flash energy and flash location are used in this study. The flash energy is the optical energy measured in a narrow 1-nm spectral band centered on 777.4 nm in units of femtojoules (10^{-15} J) (Rudlosky et al. 2019).

3) MODERATE RESOLUTION IMAGING SPECTRORADIOMETER (MODIS)

The MODIS instrument on board the polar-orbiter satellites *Terra* and *Aqua* has a viewing swath width of 2330 km. MODIS measures 36 spectral bands between 0.405 and 14.385 μm with a spatial resolution of 250–1000 m in range (Justice et al. 2002).

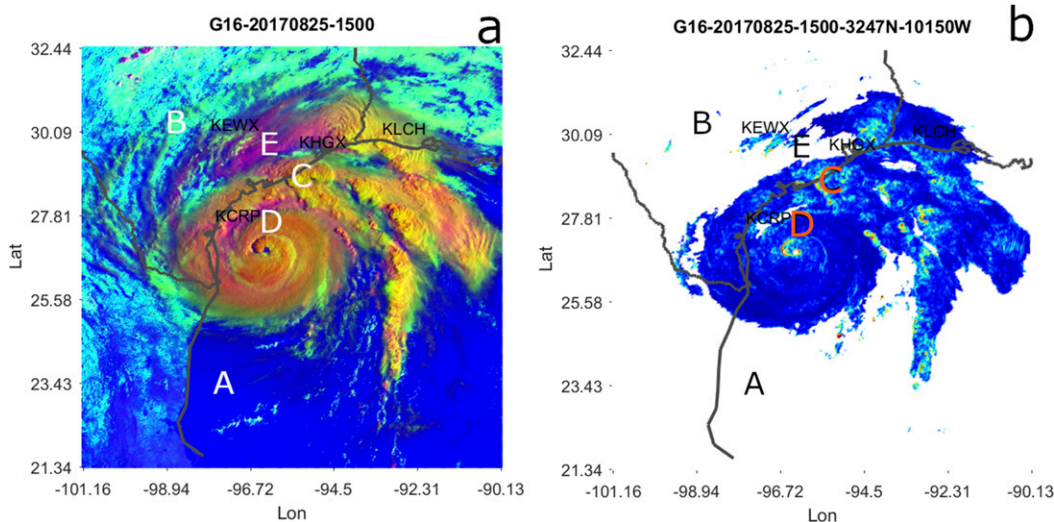


FIG. 1. (a) *GOES-16* convective RGB scheme example, and (b) corresponding roughness map, of Hurricane Harvey at 1500 UTC 25 Aug 2017. Labels A–E represent ocean (A), cirrocumulus clouds (B), deep convective clouds (C), deep nonconvective clouds (D), and nonconvective warm clouds (E).

The cloud-top effective radius r_e (μm) and cloud surface temperature T ($^{\circ}\text{C}$) retrieval are used in this study to construct T - r_e profiles as detailed in Rosenfeld and Lensky (1998), Rosenfeld et al. (2014), and Rosenfeld et al. (2016). The T - r_e profiles are used for hurricane eyewall and external rainbands microphysical similarity comparisons in this study [detailed in section 3c(2)].

b. Next-Generation Radar (NEXRAD) data and processing

1) POLARIMETRIC VARIABLES AND RETRIEVED PRODUCTS

A standard set of radar variables measured by the WSR-88D radars is used in the study. These include radar reflectivity Z , differential reflectivity Z_{DR} , specific differential phase K_{DP} , and cross-correlation coefficient ρ_{hv} . Data processing details can be found in Ryzhkov et al. (2005).

The mean volume diameter D_m and total number concentration N_t of ice particles have been estimated using polarimetric radar retrieval techniques; D_m and N_t are retrieved from the combination of Z , K_{DP} , and Z_{DR} as defined by Bukovčić et al. (2018) and Ryzhkov and Zrnić (2019). The value of D_m (mm) is determined as

$$D_m = -0.1 + 2.0 \left(\frac{Z_{\text{DP}}}{K_{\text{DP}} \lambda} \right)^{1/2}. \quad (1)$$

In Eq. (1), Z_{DP} is the reflectivity difference defined as the difference between radar reflectivity factors Z_h and Z_v at orthogonal polarizations expressed in a linear scale. Hence, the units of Z_{DP} are $\text{mm}^6 \text{m}^{-3}$. The K_{DP} is expressed in degrees per kilometer, and the radar wavelength λ is in millimeters.

The total number concentration N_t of ice particles (L^{-1}) is determined from equation

$$\log(N_t) = 0.1Z - 2 \log \left(\frac{Z_{\text{DP}}}{K_{\text{DP}} \lambda} \right) - 1.11, \quad (2)$$

where Z is expressed in reflectivity decibels (dBZ).

The advantage of using the retrieval relations in Eqs. (1) and (2) in ice is that they are little affected by the variability of the size distribution of ice and are practically insensitive to the variability of the particles' shapes and orientations (Ryzhkov and Zrnić 2019). These have been derived in the Rayleigh approximation on the assumption that the density of ice and snow is inversely proportional to the volume diameter of ice particle

$$\rho_s = \alpha D^{-1}, \quad (3)$$

where the multiplier α is proportional to the degree of riming. This means that the suggested retrieval relations are not valid in graupel or hail for which Eq. (3) is not held.

Because the measured values of K_{DP} and Z_{DR} are quite noisy in ice and snow, some additional spatial averaging of K_{DP} and Z_{DR} is needed to reduce statistical errors of their estimates. Azimuthal averaging of radar variables in a full 360° circle or in a limited azimuthal sector is at the core of recently developed techniques for processing and representing polarimetric radar variables such as quasi-vertical profiles (QVP) (Griffin et al. 2018; Ryzhkov et al. 2016; Tobin and Kumjian 2017), range-dependent QVP (or RD-QVP) (Tobin and Kumjian 2017), or enhanced vertical profile (EVP) (Bukovčić et al. 2017). The vertical profiles of major radar variables (Z , Z_{DR} , K_{DP} , and ρ_{hv}) as well as the retrieval products D_m and N_t are commonly represented in a height versus time format that allows examination of the temporal evolution of the vertical structure of the storm.

2) CVPs

QVP, RD-QVP, and EVP are radarcentric products. Murphy (2018) offers a novel technique called column-vertical profiles (CVPs) that allows estimating average vertical profiles of radar variables within a vertical column centered at an arbitrary location within the radar coverage area.

The CVP technique prescribes azimuthal averaging in a limited azimuthal sector and radial interval enclosing a center of the CVP column using all available tilts of radar data. The averaged data from each radar tilt at various distances and heights from the radar are projected along the horizontal to the vertical at the center CVP location. To create a distribution of data in the vertical that are evenly spaced with height, a Cressman averaging technique is employed. The output after this process is a single column of CVP incorporating all data at each elevation angle with varying heights at the same horizontal location in range and azimuth from the given radar. The CVP profiles are generated after every radar volume scan and displayed in a height versus time format. The selected sector in this study spans 20 km in range and 20° in azimuth around the center of the selected CVP column. The locations of the selected CVP columns are shown with white squares in Fig. 2. The CVP time resolution is determined by the radar volume update time of 5 min. Detailed CVP method description can be found in Murphy (2018). The track of Harvey's eye is shown in Fig. 2a as it moves closer and passes by the CVP location. (The remaining panels in Fig. 2 do not

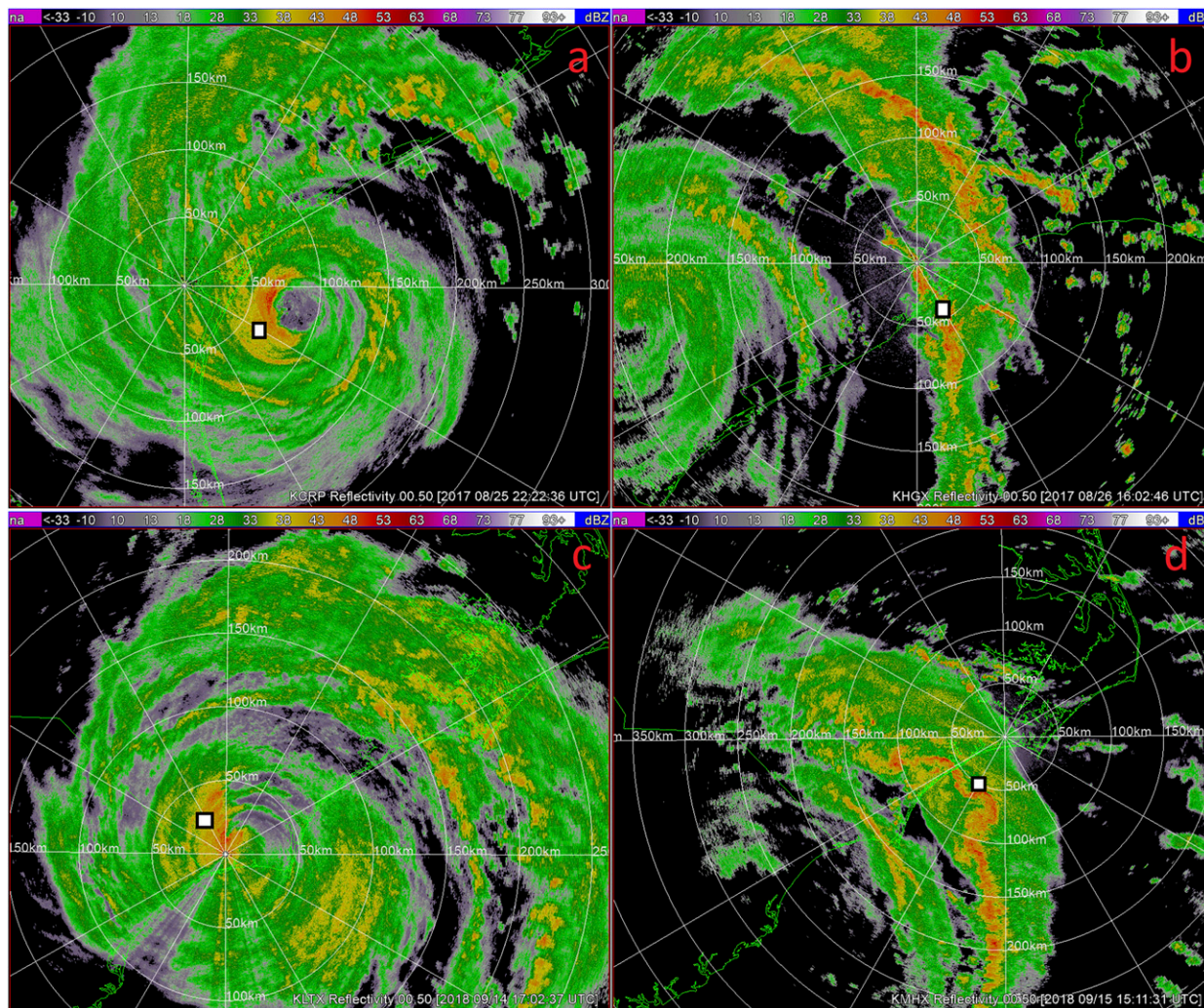


FIG. 2. Radar 0.5° reflectivity plan position indicator (PPI) maps: (a) Harvey’s inner eyewall, (b) Harvey’s outer rainband, (c) Florence’s inner eyewall, and (d) Florence’s outer rainband. Radar CVP areas are labeled by the white boxes in all radar PPI panels.

need such marking since the storms are relatively stationary in Figs. 2b–d.)

c. *Lightning Mapping Array (LMA)*

The Houston LMA consists of 12 time-of-arrival lightning sensors operating in the very high frequency (VHF) television band (e.g., 60–66 MHz) and using the time of arrival events at each LMA site to produce three-dimensional lightning discharges dataset. The temporal and spatial resolutions of LMA are 80 μs and 10⁻⁶° (Cullen 2013). The quality control is to exclude data points with chi-square values of their triangulation less than 1.0 (Cullen 2013). The integrated event counts are prepared for each CVP time–height pixel with the same spatial and temporal resolution.

d. *High-Resolution Rapid Refresh (HRRR) model data*

The HRRR is a National Oceanic and Atmospheric Administration (NOAA) real-time atmospheric model with 3-km resolution and hourly update initialized by 3 km grids with 3 km radar assimilation (Benjamin et al. 2016). 3D radar reflectivity is assimilated in the HRRR every 15 min over a 1-h period adding detail to that provided by the hourly data assimilation from the 13 km resolution radar-enhanced Rapid Refresh simulations (Benjamin et al. 2016; Peckham et al. 2016). The hourly updated HRRR data give the estimate of the 0°, –15°, and –40°C isotherms’ heights. The closest HRRR data point to the CVP location center is used to depict the heights of the isotherms.

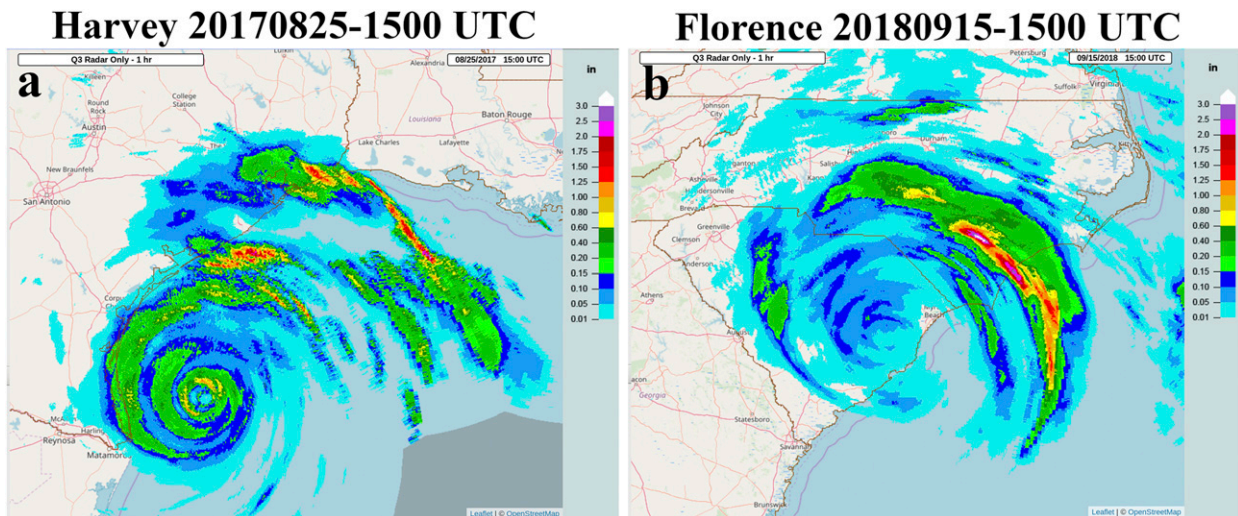


FIG. 3. The 1-h cumulative radar QPEs from MRMS for (a) Harvey for 1500–1600 UTC 25 Aug 2017 and (b) Florence for 1500–1600 UTC 15 Sep 2018.

e. Multi-Radar Multi-Sensor (MRMS) platform

The MRMS platform developed at the National Severe Storm Laboratory provides quantitative precipitation estimation (QPE) products on the WSR-88D network (Zhang et al. 2016). One of the available QPE products is radar based with local gauge bias correction. This QPE product's spatial and temporal resolutions are 1 km and 2 min, respectively. The 1-h cumulative precipitation estimates from MRMS QPE are utilized in this study.

3. Results

a. 1-h radar QPEs of Harvey and Florence

Figure 3a shows the 1-h radar QPE of Harvey on 25 August 2017 from 1400 to 1500 UTC. The eyewall region (the green circular areas around the eye of hurricane) precipitation rate is less than 20 mm h^{-1} . The external rainband is located outside the main circulation on the northeast side of the hurricane. The maximum precipitation hourly accumulation rate exceeds 60 mm h^{-1} (the red areas within the external rainbands), which is high enough to potentially produce flooding if sustained for a sufficiently long time. A similar pattern is found in Florence (Fig. 3b) on 15 September 2018 from 1400 to 1500 UTC, in which the external rainband peak hourly accumulation rate ($>70 \text{ mm h}^{-1}$) is 20 times that within the inner eyewall region ($<4 \text{ mm h}^{-1}$) (Blake and Zelinsky 2018). This raises the question of what processes might be responsible for the large difference in precipitation intensities between the eyewall and external rainbands regions.

b. Radar investigation of storm structure

1) WSR-88D CVP OBSERVATIONS IN HARVEY AND FLORENCE

The investigations of the storms' structure are performed using WSR-88D CVPs. Figure 4 shows the CVPs of Z , Z_{DR} , K_{DP} , and ρ_{hv} and retrieved parameters of size distributions D_m and N_t observed close to the eye of Harvey from 1500 to 2211 UTC 25 August 2017. A ρ_{hv} depression at the height around 5 km defines the melting-layer (ML) signature in polarimetric CVPs (Fig. 4d). The CVP of reflectivity from 1829 to 2000 UTC below the ML shows increasing rain intensity toward the surface. Such reflectivity gradient combined with downward increasing K_{DP} (Fig. 4c) indicates that the surface precipitation is dominated by warm-rain processes. Based on all previous observations, this distinct warm-rain mechanism within the eyewall region usually produces moderate to heavy precipitation, but not as extremely heavy as in the external rainbands, which are discussed next. The overall reflectivity (Fig. 4a) is lower than 20 dBZ above the ML and the ρ_{hv} ML signature is uninterrupted, which indicates weak vertical motions and a nonconvective nature of precipitation in this CVP area (Proctor and Switzer 2016). Note that the D_m and N_t retrieval algorithms specified by Eqs. (1) and (2) work for pure ice phase only, and the D_m and N_t estimates are not made within the ML. Above the -15°C isotherm, ice crystals are small (with D_m varying from 0.1 to 0.5 mm) and their total concentration is high (up to 10^3 L^{-1}).

The CVPs of the external rainband are shown in Fig. 5. The ML identified by ρ_{hv} (Fig. 5d) is also at

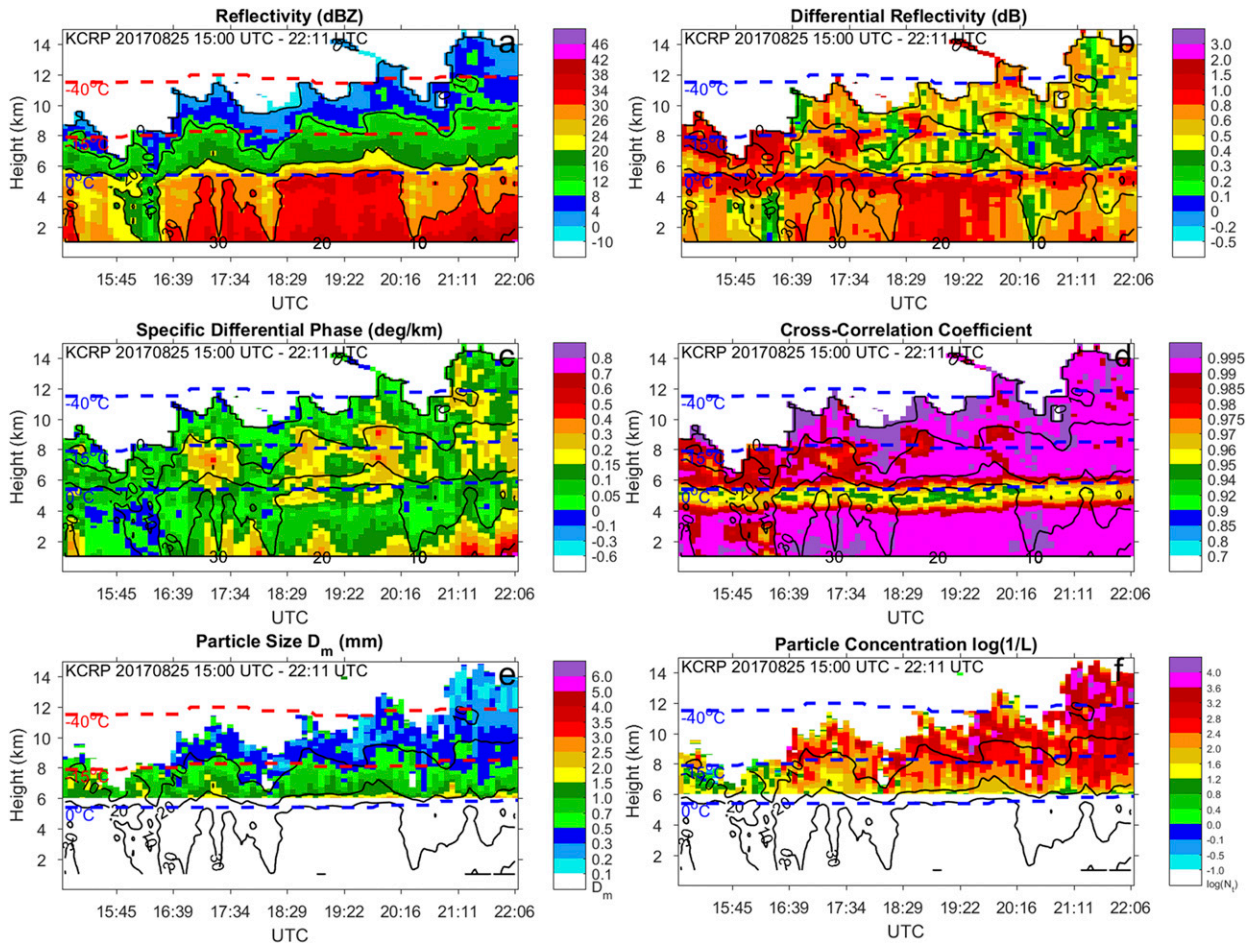


FIG. 4. CVP of (a) Z , (b) Z_{DR} , (c) K_{DP} , (d) ρ_{hv} , (e) D_m , and (f) N_r in the Hurricane Harvey eyewall region from 1500 to 2211 UTC 25 Aug 2017. The CVP is centered at 60 km and 120° from the KCRP WSR-88D, and the CVP base is 20 km in range and 20° in azimuth. The black contours are drawn every 10 dBZ and are the same in each panel. The dashed lines in each panel show the corresponding 0°, -15°, and -40°C isotherms from HRRR.

around 5 km height. A black box in each panel encloses the maximum K_{DP} (Fig. 5c) region, which represents maximum precipitation. The downward positive gradient of Z , Z_{DR} , and K_{DP} below the ML from 1543 to 1630 UTC indicates further enhancement of the precipitation by raindrop coalescence (Ryzhkov and Zrnić 2019). High values of Z (Fig. 5a) and Z_{DR} (Fig. 5b) within black boxes indicate heavy precipitation. The magnitude of ρ_{hv} in the ML is higher in the convective region and represents a common indication of melting graupel or heavily rimed snow (Fig. 5d). As opposed to the eyewall region, Z above the ML exceeds 20 dBZ (Fig. 5a). The combination of these features shows the convective nature of precipitation in this CVP area of the storm that produces heavy precipitation (38 mm hourly accumulation from radar QPEs). Besides a coalescence process, size sorting by relatively strong vertical motion documented by Wu et al. (2018) can also result

in positive downward gradient of Z_{DR} . Because of relatively large Z (>20 dBZ; Fig. 5a) and almost zero K_{DP} (Fig. 5c) between the red and black boxes, the ice-phase hydrometers here are likely composed of highly aggregated snow and graupel. The red numbers at the bottom represent a GLM flash number count in a logarithmic scale in this CVP region. The occurrence of lightning is consistent with the development of convection here. Interestingly, no GLM lightning flashes were detected in Harvey’s eyewall within the selected CVP area.

In Fig. 6, the Houston LMA data are reconstructed to the identical time–height grids as in the CVP columns shown in Fig. 5. The red box is selected around the core of maximum LMA source count. The core of peak LMA counts (up to 10^{11} events per CVP pixel) is between the -15° and -40°C isotherms. The red box in Fig. 5 is at the same location as in Fig. 6. Low Z (Fig. 5a; <20 dBZ), high Z_{DR} (Fig. 5b; >0.4 dB) and high K_{DP}

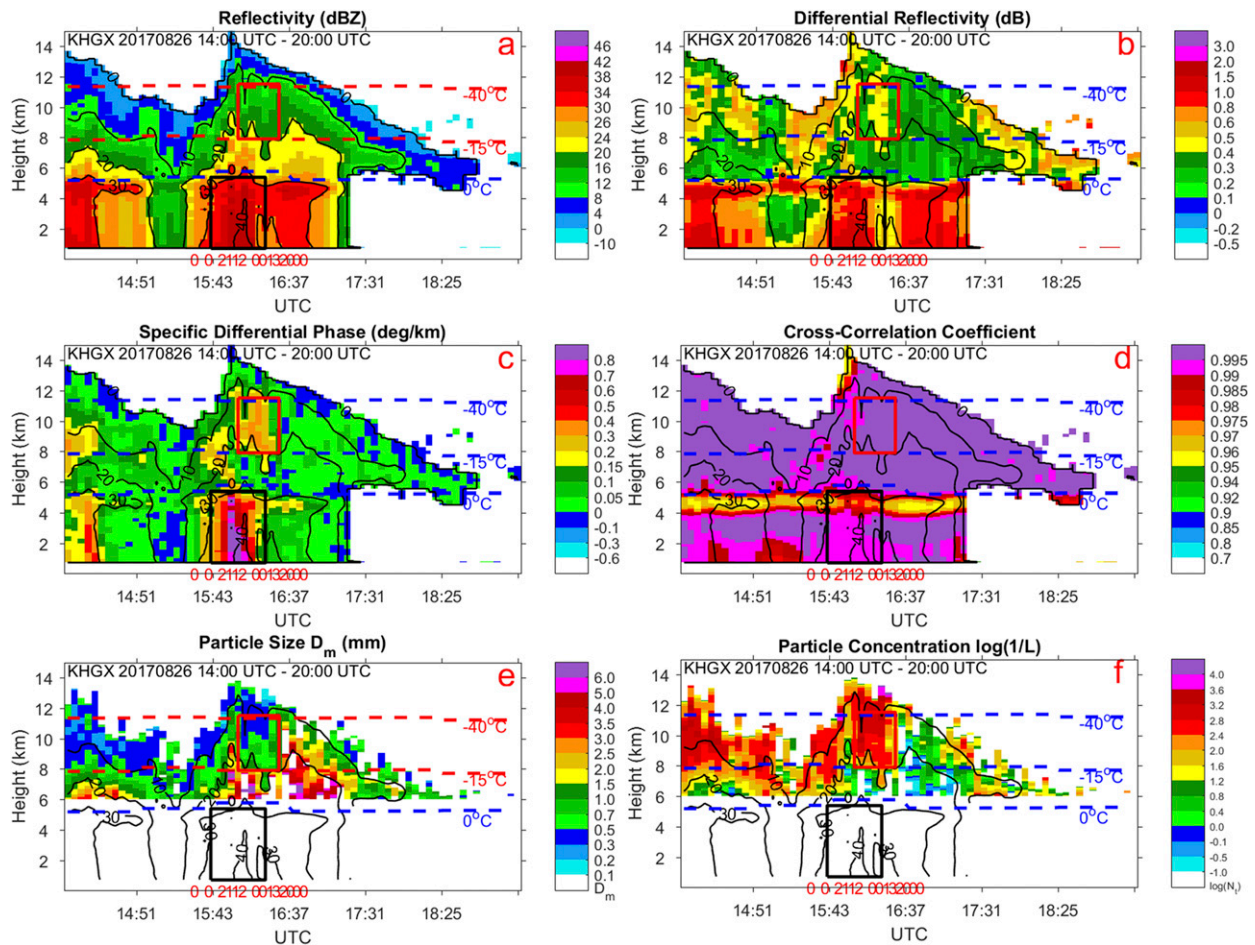


FIG. 5. As in Fig. 4, but for Hurricane Harvey's external rainbands from 1400 to 2000 UTC 26 Aug 2017. The CVP is centered at 40 km and 150° from the KHGX WSR-88D. The red numbers at the bottom of each panel indicate a GLM flash count expressed in a logarithmic scale (log to the base 2) within the CVP area in each radar volume scan.

(Fig. 5c; $>0.3^\circ \text{ km}^{-1}$) within the red boxes indicate large amount of small ice crystals. The low D_m (Fig. 5e; 0.3–1 mm) and high N_t (Fig. 5f; over 10^3 L^{-1}) signature within the red boxes further prove the existence of high concentration of small ice crystals. The traditional charge separation mechanism implies that the prerequisite environment must include ice crystals, graupel and supercooled water (Williams 1989). While a direct radar retrieval of supercooled water is not possible, the coexistence of ice crystals, graupel, and the core of lightning flashes suggests the presence of supercooled water. The peak of lightning is slightly lagged in time (~ 20 min) after the maximum updraft at the lower levels (black box), which may indicate that some time is needed for convection development and ice-phase hydrometeor formation at higher altitude.

The CVP plots of the eyewall of Florence are shown in Fig. 7, from 1500 to 2000 UTC 14 September 2018. The ML around 5 km is less pronounced in the ρ_{hv} panel

(Fig. 7d) than in the Harvey case. The temporal evolution of the Z , Z_{DR} , and K_{DP} patterns from 1646 to 1929 UTC suggest heavy precipitation (Figs. 7a–c). The nonconvective tropical warm rain dominates in the Florence eyewall region and is represented by the

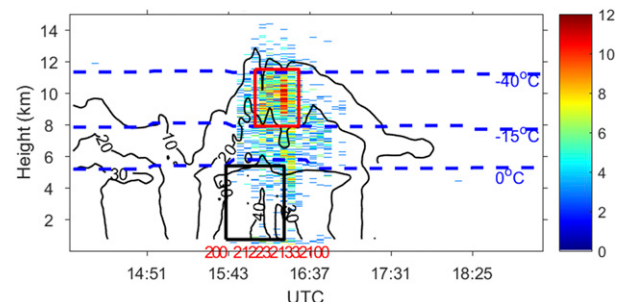


FIG. 6. LMA source count (dB) within the same CVP area as in Fig. 5 with identical temporal and spatial resolution. Overlaid are the isotherms and reflectivity contours (dBZ).

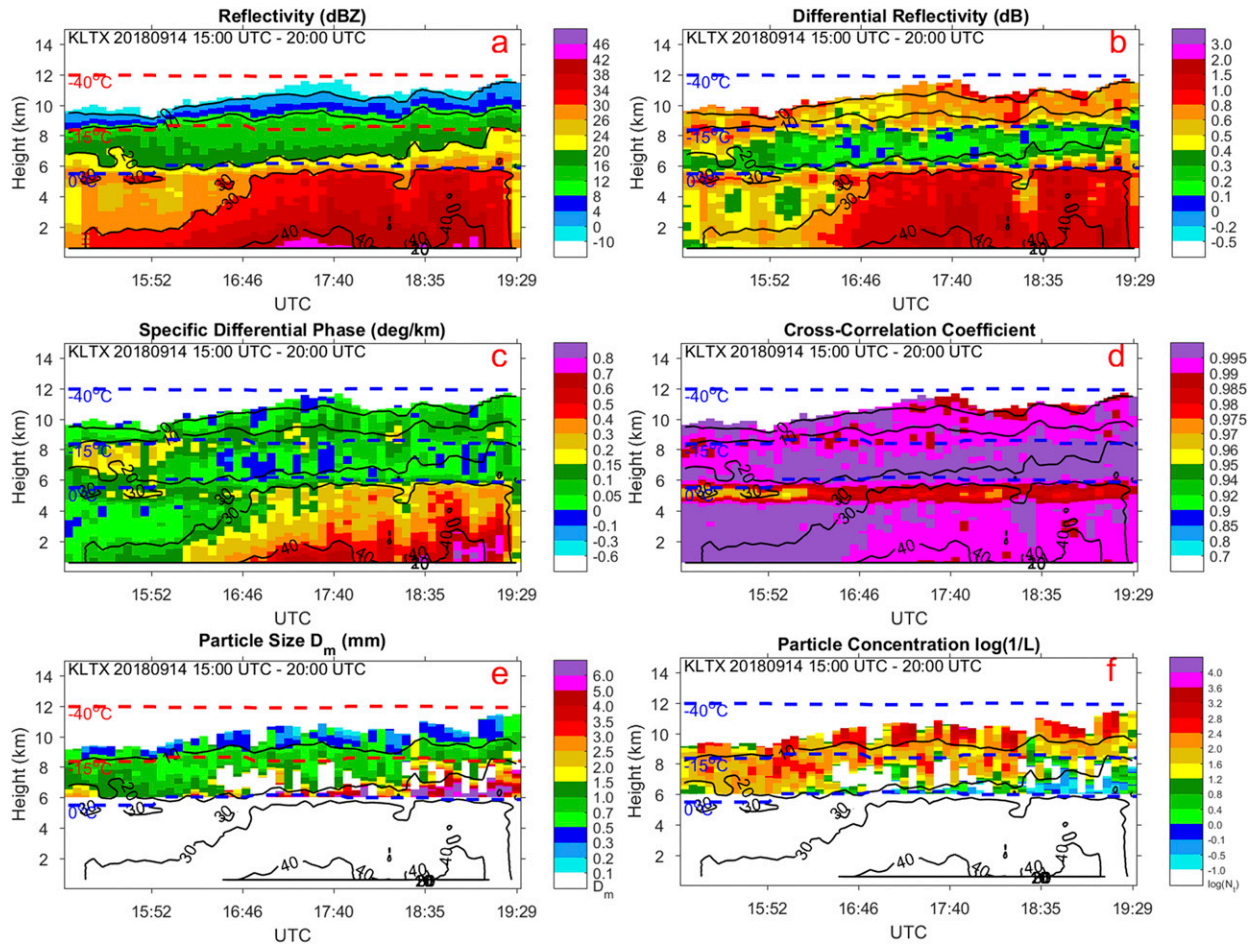


FIG. 7. As in Fig. 4, but for the Hurricane Florence’s eyewall from 1500 to 2000 UTC 14 Sep 2018. The CVP is centered at 28 km and 330° from the KLTX WSR-88D.

combination of relatively low Z (Fig. 7a; <20 dBZ) above the ML and high vertical gradients of Z and K_{DP} below the ML (Figs. 8a,c). The tropical warm-rain processes in the CVP area of the Florence eyewall region are more pronounced than that in the same region of Harvey but are still much weaker than in the external convective rainbands. Lack of GLM flash count within this CVP region further confirms its weak convective nature above the ML.

The CVPs in the external rainbands of Florence are shown in Fig. 8, from 1500 to 1912 UTC 15 September 2018. Note that the WSR-88D radar at the KMHX site observation stopped working at 1912 UTC due to the system failure. The ML is well defined in the ρ_{hv} panel (Fig. 8d) around 5 km. The black box contains an intense K_{DP} (Fig. 8c) shaft from 1510 to 1535 UTC below the ML. Within the same time slot, Z (Fig. 8a) above the ML shows a convective signature of $Z > 20$ dBZ stretching up to 10 km. The ρ_{hv} depression in the ML within the black box (Fig. 8d) is less pronounced likely

due to a stronger updraft and melting ice hydrometeors with higher density falling through. The convective feature within this CVP sector is similar to the Harvey external rainband (Fig. 5). The strong K_{DP} (Fig. 8c; $>0.6^{\circ} \text{ km}^{-1}$) shaft and almost homogeneous Z_{DR} (Fig. 8b; 0.6–0.8 dB) indicates that the growth of raindrops by either coalescence or accretion below the ML is masked by the contribution from raindrops originating from ice aloft.

The red box denotes a possible lightning core in this convective CVP time–height series. LMA data are not available for Florence, but the GLM shows some lightning activity there. The red box also encloses the area of high concentration of small ice crystals with low Z (Fig. 8a; <20 dBZ), relatively high Z_{DR} (Fig. 8b; >0.4 dB) and relatively high K_{DP} (Fig. 8c; $>0.3^{\circ} \text{ km}^{-1}$). Between the red and black boxes, Z (Fig. 8a) is over 20 dBZ and K_{DP} (Fig. 8c) is close to 0, which indicates the existence of graupel. The coexistence of ice crystals, graupel, and strong vertical motion implies the

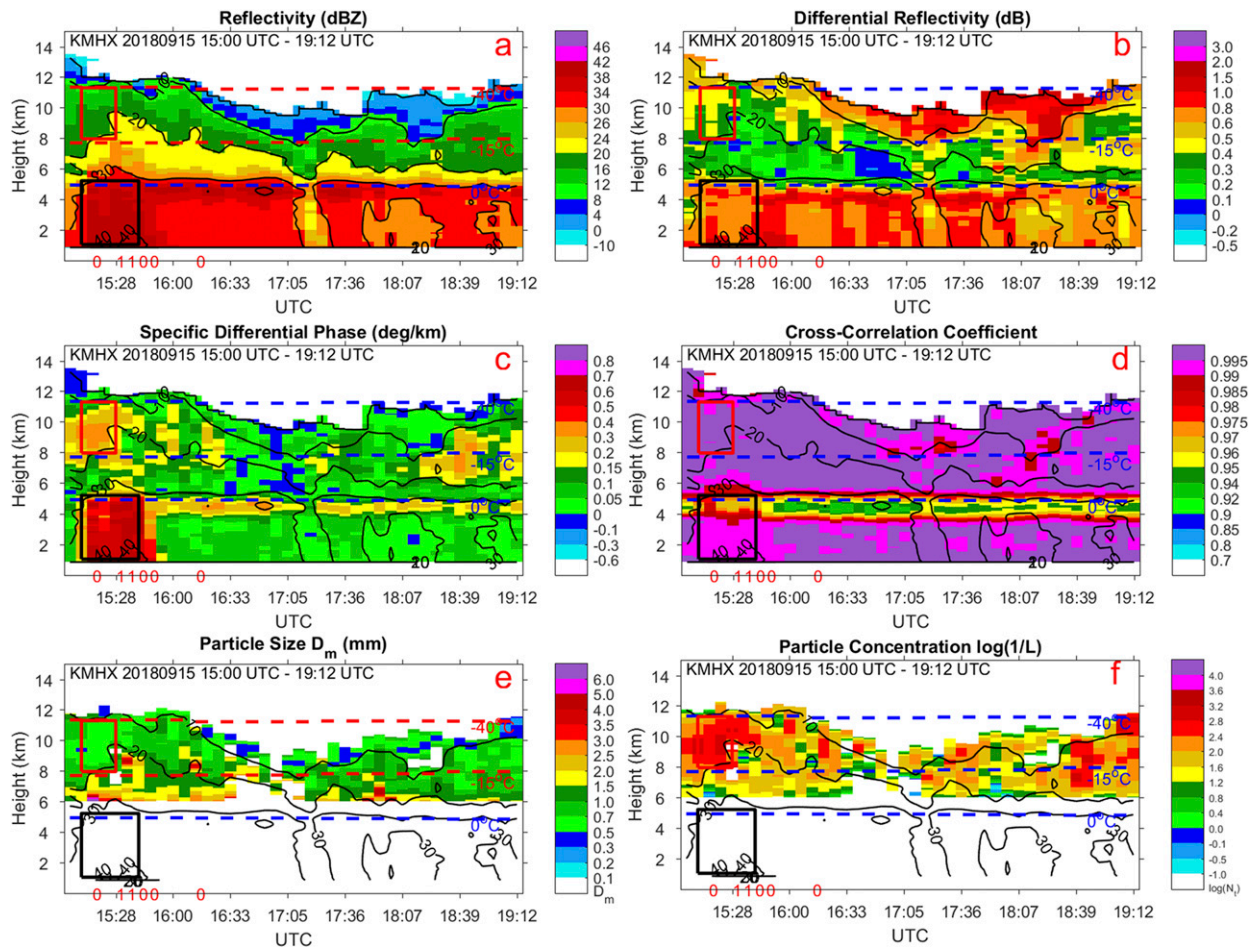


FIG. 8. As in Fig. 5, but for Hurricane Florence external rainbands from 1500 to 1912 UTC 15 Sep 2018. The CVP is centered at 50 km and 210° from the KMHX.

transportation of supercooled water upward, favoring cloud electrification that is identified by the GLM data.

2) EVIDENCE OF SIZE SORTING RELATED TO WIND SHEAR

Raindrop size sorting (Didlake and Kumjian 2018; Feng and Bell 2019) is commonly manifested by the displacement of the maximum of Z_{DR} with respect to collocated maxima in Z and K_{DP} (Kumjian and Ryzhkov 2012; Dawson et al. 2015; Didlake and Kumjian 2017; Ryzhkov and Zrnić 2019). Such a pattern is evident in the PPI at 0.5° elevation of the KCRP (Corpus Christi WSR-88D) radar data in the Harvey eyewall region shown in Fig. 9. The prominent maxima of Z , Z_{DR} , and K_{DP} are marked by white contours (Figs. 9a–c). In the eyewall region, the Z (Fig. 9a) and K_{DP} (Fig. 9b) enhancements are well collocated, whereas the Z_{DR} maximum region (Fig. 9c) is located at the northeast upwind region of the eyewall. Such asymmetry of the Z_{DR} pattern with respect to those of Z and K_{DP} can be explained

by raindrop size sorting caused by wind shear (Kumjian and Ryzhkov 2012) or by the significant storm-relative wind (Dawson et al. 2015). Smaller raindrops have lower terminal velocities compared to larger raindrops. A strong wind shear near the eyewall region creates more intense storm-relative flow. Smaller raindrops are advected farther downstream than fewer larger raindrops, which causes decorrelation of Z_{DR} with Z and K_{DP} . The shift is very large, about 60° around the eyewall, thus representing a respectively large local storm wind shear. The external rainbands exhibit no such shifts of the Z_{DR} maxima with respect to the Z and K_{DP} cores, as shown in Figs. 9d–f. This is likely due to much weaker wind speed and local storm wind shear, which do not facilitate the size sorting process. Hurricane Florence exhibits similar patterns (not shown here), although the polarimetric size sorting signature is not as pronounced as in Harvey. In general, wind shear between maximum wind velocity (altitude around 1–2 km) and homogenous freezing level (altitude around 12 km) at the eyewall

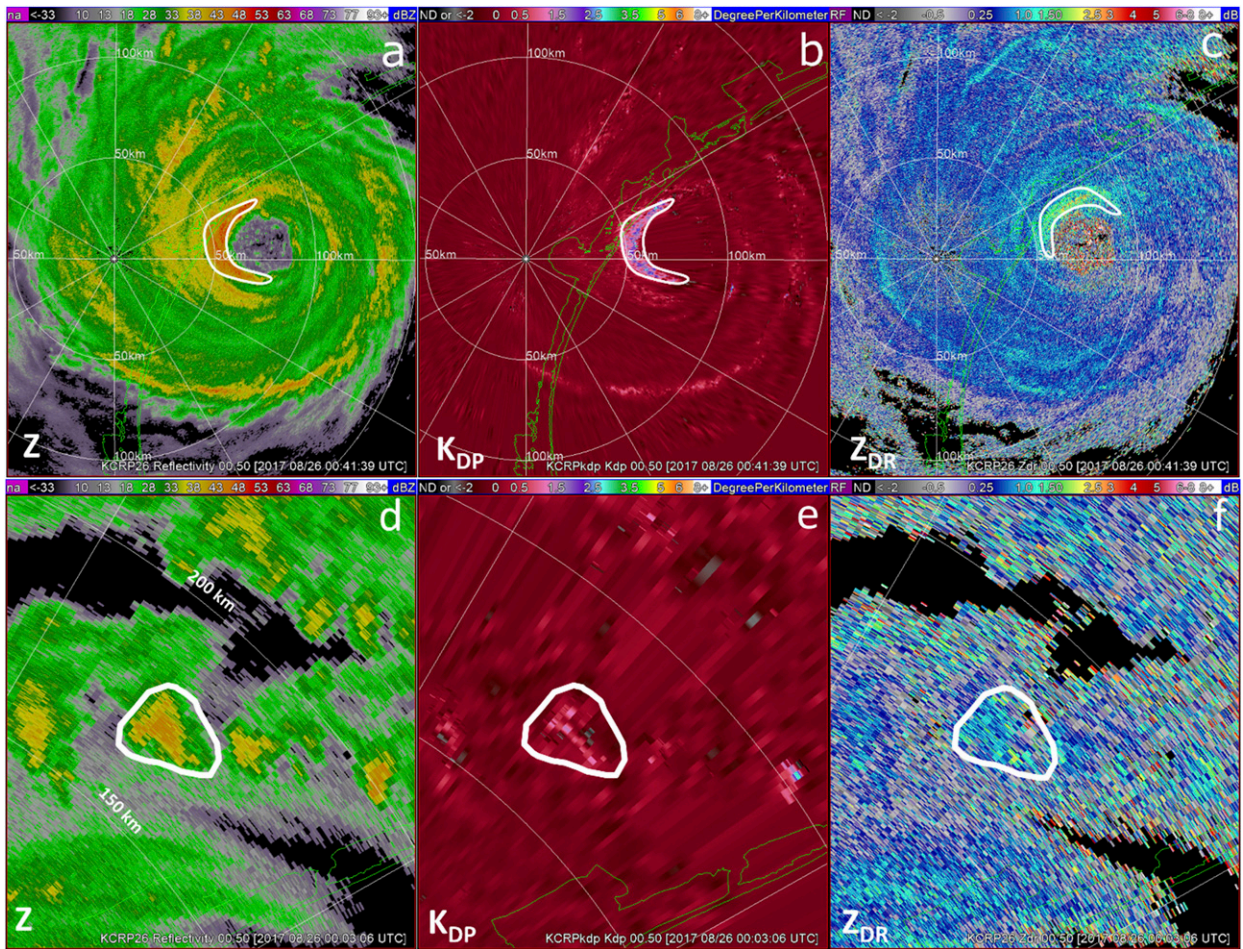


FIG. 9. KCRP PPIs of Harvey at 0.5° near Corpus Christi: (a),(d) Z; (b),(e) K_{DP} ; and (c),(f) Z_{DR} (top) near the eyewall region at 0041 UTC and (bottom) in external rainbands at 0003 UTC 26 Aug 2017. White contours enclose Z, Z_{DR} , and K_{DP} maxima.

regions is at least 2 times that in the external rainband regions in both hurricanes (shown in Fig. 12).

c. Satellite investigation of storm structure

1) GOES-16 OBSERVATIONS OF HARVEY AND FLORENCE

Radar observes detailed microphysical structure differences between eyewall region and external rainbands within the clouds' vertical columns, but it may have insufficient sensitivity to capture the storm structure near cloud tops. The satellite can complement radar data by distinguishing the regions of intense and weak convection.

The convective RGB scheme was applied to Hurricanes Harvey and Florence, as shown in Fig. 10. Figure 10a is a snapshot of Harvey over an open ocean at 1500 UTC 24 August 2017 with the GLM data overlaid at the same time in Fig. 10b. The eye was not obvious at this time (Figs. 10a,b) because Harvey was quickly intensifying

and large mass of deep convection formed over the center (Blake and Zelinsky 2018). This can be inferred from the yellow, rough cloud-top signatures by the east eyewall region. The added GLM flash dots over this region further confirm its strong convective nature.

Late on 24 August, Harvey intensified into category-3 hurricane with a clear eye (not shown here). The next day, Harvey further intensified into category 4 and reached the Texas coastline (Figs. 4c,d). From the snapshot at 1500 UTC 25 August 2017, a clear eye and eyewall region with smooth cloud tops develops. This appearance implies no penetrating strong updrafts overshooting from the cloud tops. The external rainbands in Fig. 10c are marked by high roughness signatures and are highly convective. Figure 10d with GLM flash data overlaid shows a clear distinction between convective external rainbands and weaker convective inner core region. The updrafts in the eyewall may have been suppressed by the strong vertical wind shear,

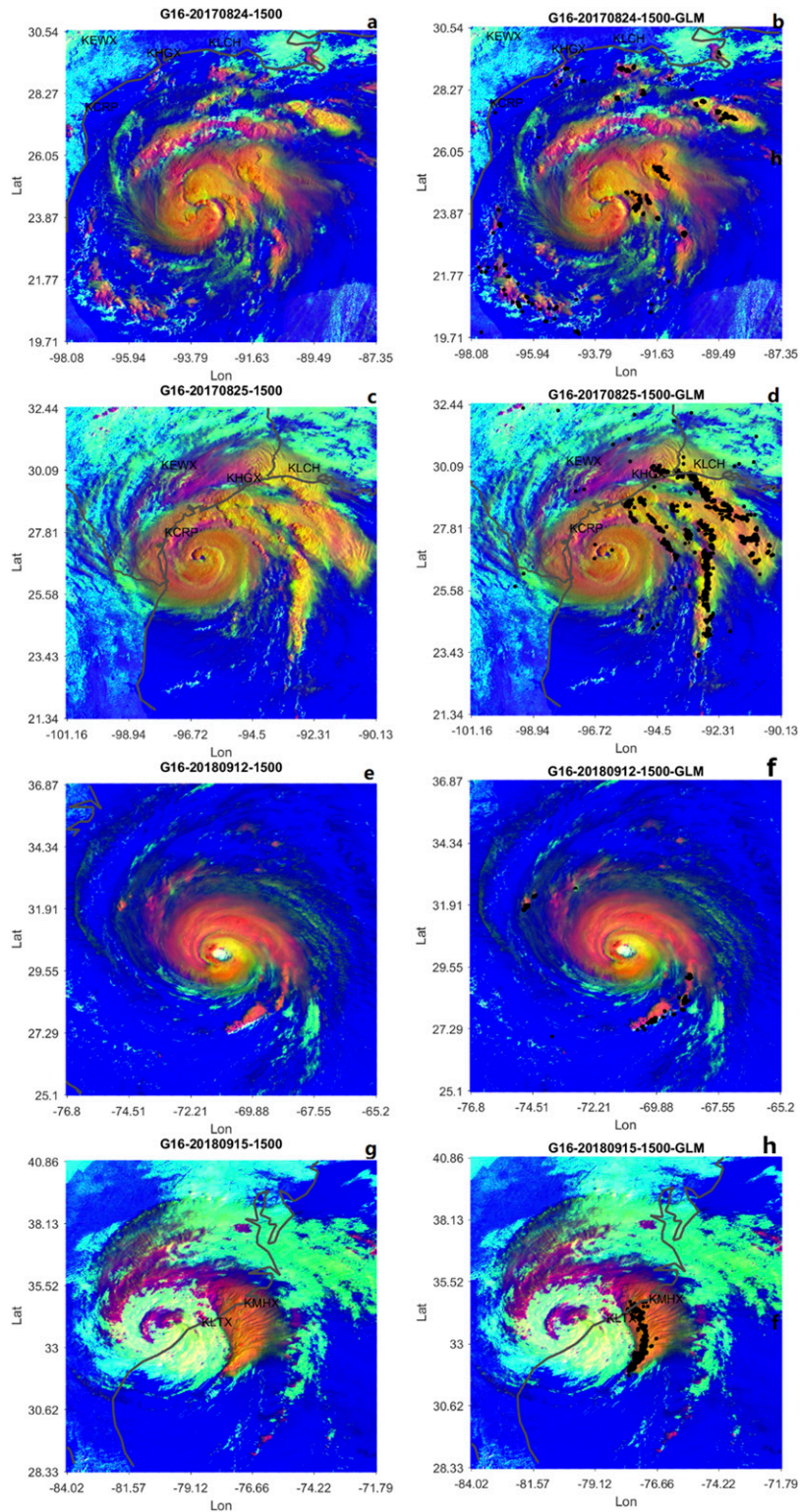


FIG. 10. *GOES-16* convective RGB snapshots of Hurricanes (a)–(d) Harvey and (e)–(h) Florence for (left) RGB snapshots only and (right) RGB snapshots with GLM data. Each black dot represents one GLM flash data point.

inhibiting very strong vertical motions. The external rainbands that reside outside of the main hurricane circulation intensify maintain their highly convective nature.

Hurricane Florence quickly formed and intensified as a category-4 hurricane over the open Atlantic Ocean on 12 September 2018, as shown in Figs. 10e and 10f. The hurricane maintained its strength over ocean. The eyewall region shows no sign of overshooting and is mostly nonconvective. Only the southeast tail of Florence in these snapshots (Figs. 10e,f) shows some convective signatures as can be validated by the GLM flash dots overlaid (Fig. 10f).

From 14 to 15 September 2018, Florence moved slowly along the coastline of North Carolina and produced extensive flooding along the way. Figures 10g and 10h show snapshots of Florence at 1500 UTC 15 September 2018. The hurricane eye is too ill defined to be seen, but the external rainband denoted by the bright yellow region is highly convective and produced large amount of precipitation (Zhang et al. 2018). Flash density and cloud-top roughness can be used as indicators of strong updrafts and, likely, heavy precipitation. Florence and Harvey have comparable convective strength of their external rainbands. They both produced heavy flooding within the rainbands.

2) MODIS $T-r_e$ PROFILES IN THE EYEWALL VERSUS EXTERNAL RAINBANDS

To further investigate the hurricane cloud-top features, MODIS $T-r_e$ profiles of Harvey at 1725 UTC 25 August 2017 are shown in Fig. 11. The retrieval technique for $T-r_e$ profiles is described by Rosenfeld et al. (2016) and Zhu et al. (2014). This profile shows cloud-top particles' effective radius at various heights within each selected region (eyewall or external rainbands). The pixels within each selected region are assumed to be within a similar air mass environment and follow similar vertical growth pathways. In this representation, the temporal evolution of the clouds is obtained by snapshots of cloud ensembles at different stages in their life cycle (Lensky and Rosenfeld 2006). (The location of each of the selected regions is shown in Fig. S1 in the online supplemental material.)

The light-blue solid line shows that the external rainband's cloud base starts near 20°C. The jump in r_e at -10°C indicates the onset of glaciation. The decrease in r_e above the -25°C isotherm indicates formation of smaller ice particles, probably as a result of additional nucleation of cloud droplets that freeze to ice particles. The accelerated decrease in r_e above the -40°C isotherm indicates additional creation of small ice particles, possibly due to activation of ultrafine aerosol particles

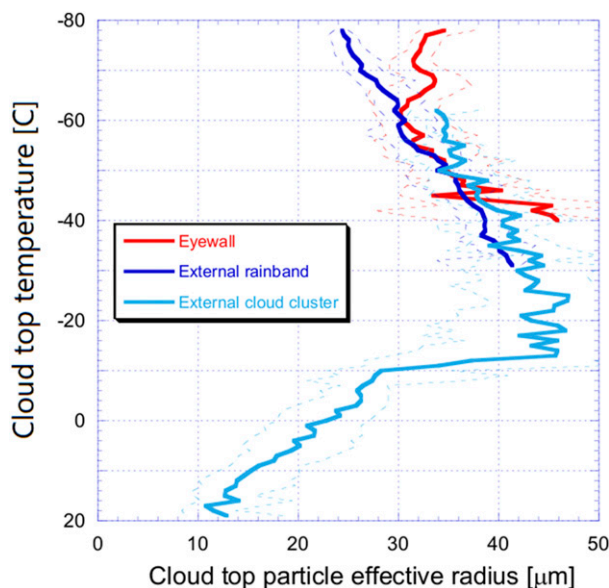


FIG. 11. MODIS $T-r_e$ profiles of Harvey inner eyewall (red lines) and external rainbands (blue lines). The solid lines represent the 50th percentile of each region's data points. The left dashed line at each corresponding solid line is the 15th percentile of each region's data points, and the right dashed line is the 85th percentile of each region's data points. The regions are shown in Figs. S1 and S2 in the online supplemental material.

in the high supersaturation created by strong updrafts (Fan et al. 2018; Khain et al. 2012). The selected external rainband (dark blue solid line) and eyewall (red solid line) regions are mainly characterized by cloud pixels colder than -35°C, which means only the homogenous freezing process dominates here. The external cloud cluster (light-blue solid line) profile gives a more complete picture of how cloud particles evolve with height at lower altitude. By comparing the eyewall (red solid line) and external rainband (dark-blue line) profiles, the clouds in both regions reach similar height or top temperature (around -80°C). The r_e at the external rainbands cloud top is roughly 10 μm smaller than at the eyewall cloud top. Generally smaller cloud-top r_e at the external rainband indicates stronger updraft and transport of smaller secondary activated aerosols [likely from ultrafine aerosol particles (UAPs)] to cloud top. We hypothesize that the stronger wind shear in the eyewall region impedes the updrafts. This will be discussed in section 4.

d. HRRR wind shear analysis

The HRRR model assimilates radar data combined with the gridpoint statistical interpolation assimilated cloud and hydrometeor data, which provides significant skills in short term forecast and is used here for wind shear analysis.

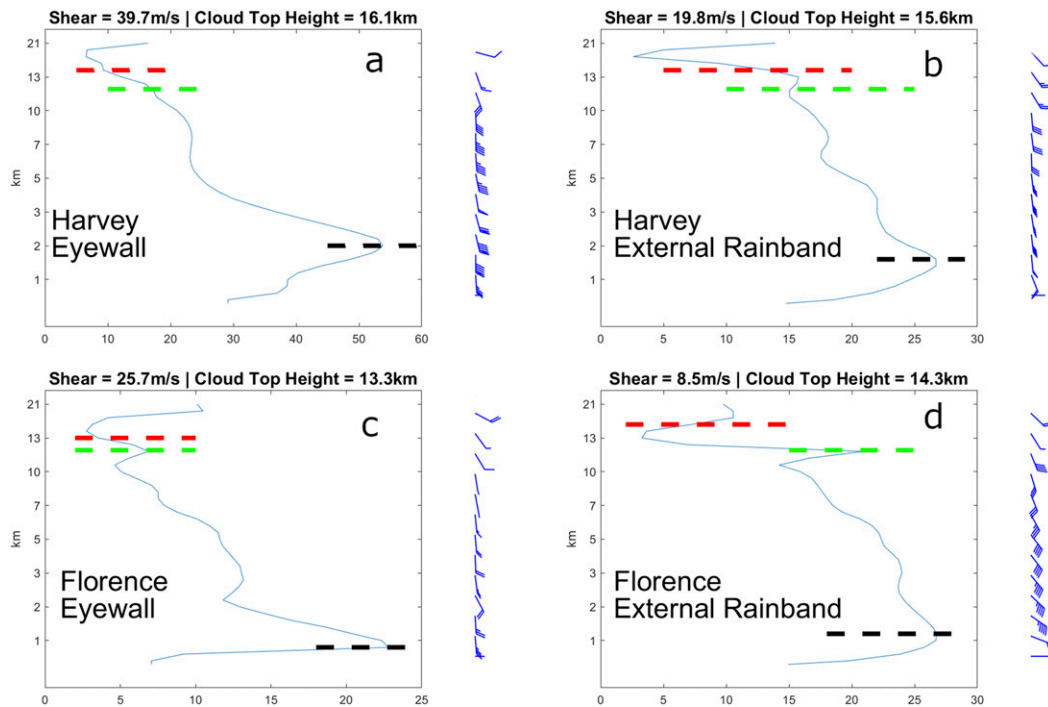


FIG. 12. Vertical wind profiles and wind barbs of (a),(b) Harvey and (c),(d) Florence at both (left) inner eyewall and (right) external rainbands. Vertical maximum wind velocity layer, homogenous freezing level, and cloud-top layer are represented by dotted black, green, and red lines, respectively. The x axis shows temperature in Celsius, and the y axis shows height in kilometers.

The HRRR model vertical wind profiles of Harvey and Florence in the inner eyewalls and external rainbands are shown in Fig. 12. The location of each vertical wind profile is at the center of each CVP sector shown in Figs. 4–8. The timing of the eyewall snapshots is selected in such a way that the center of the hurricanes is closest to each selected CVP central point, that is, at 2000 UTC 25 August 2017 for Harvey (Fig. 12a) and at 1800 UTC 14 September 2018 for Florence (Fig. 12c). The times for the external rainbands are selected when the strongest convective signatures occur (detailed in section 3b), that is, at 1600 UTC 26 August 2017 for Harvey (Fig. 12b) and at 1500 UTC 15 September 2018 for Florence (Fig. 11d). Wind shear (wind velocity differences between layers) is calculated between the height of maximum wind velocity (dotted black line) and homogenous freezing level (dotted green line). The homogeneous freezing level is at the -40°C isotherm calculated by HRRR. The choice of reference levels for wind shear calculation is dictated by the need to examine the maximum wind speed difference between lower altitude and homogeneous freezing level, where the aerosol effects matter most (Iltoviz et al. 2016). The Harvey's inner rainband wind shear (Fig. 12a, 39.7 m s^{-1}) is 2 times that in the external rainband (Fig. 12b, 19.8 m s^{-1}), and

Florence's inner rainband wind shear (Fig. 12c, 25.7 m s^{-1}) is 3 times that in the external rainband (Fig. 12d, 8.5 m s^{-1}). In general, wind shear is stronger at the inner rainbands than in the external rainbands. The stronger shear in the eyewall region may tilt and suppress the updraft, thus weakening local vertical transport and spreading it along the rainband. Since wind barbs show little change of direction, directional shear probably plays a less important role here.

4. Conceptual model and hypothesis

From the results of our observations, the following conceptual model can be suggested. In this conceptual model (Fig. 13), the hurricane eyewall region (Fig. 13a) has strong vertical wind shear that significantly weakens vertical motion and tilts the cloud hydrometeors' transport pathway (Fan et al. 2009), which is further confirmed by the decorrelation of Z_{DR} with Z and K_{DP} within the eyewall region described in section 3b(2). The $T-r_e$ profiles comparisons in section 3c(2) also indicate that stronger wind shear impedes vertical transport of smaller secondary activated aerosols aloft near the eyewall. The aerosols near eyewall are composed mainly of a very wide spectrum of sea spray. The large

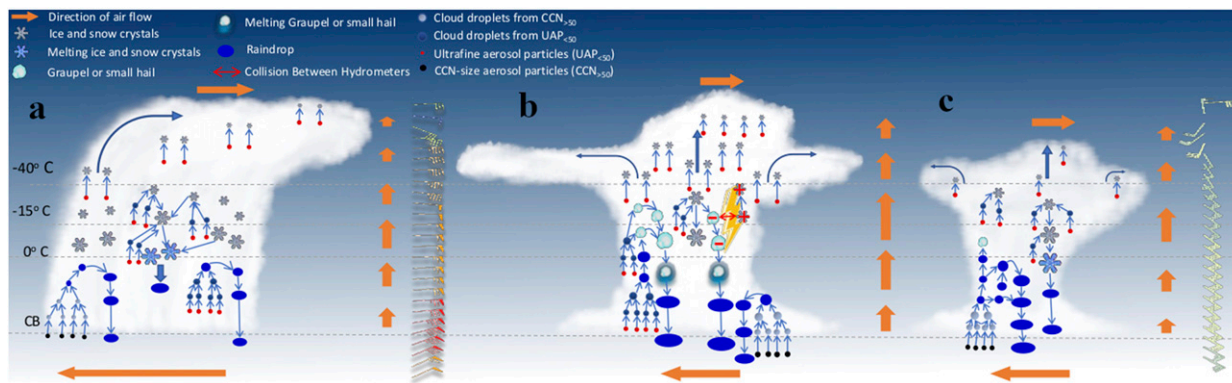


FIG. 13. Conceptual models of (a) the hurricane eyewall cloud and of external convective bands with (b) large concentrations and (c) low concentrations of UAPs. In the eyewall clouds, the strong vertical wind shear greatly weakens vertical motions and tilts cloud vertical development. The strong horizontal wind produces heavy sea spray that includes large concentrations of UAPs, which activate aloft and create high concentrations of small ice crystals. Surface precipitation is dominated by warm rain. The clouds in the external rainbands with high UAPs from industrial activities release large amount of condensational heating aloft and further invigorate convection. The enhanced ice formation includes high concentrations of small ice particles at cloud top and hail/graupel at the supercooled levels, which likely induce lightning activities. Heavy mixed-phase precipitation dominates and poses a severe risk of flooding. For the low UAP in the external rainband clouds, the convection strength is weaker than in the high-UAP scenario. The corresponding precipitation rate, cloud vertical development, and chance of lightning activities are decreased, respectively.

particles lower the cloud-base supersaturation and prevent the UAPs from nucleating cloud drops at its base (Shpund et al. 2019). Large number of UAPs are activated further aloft via in-cloud nucleation and produce a high concentration of small cloud droplets (Pinsky and Khain 2018). These small liquid droplets glaciate at low temperatures, particularly above the homogeneous ice nucleation level, and give rise to a large number of small ice crystals in the upper part of the cloud. The precipitation in this region is dominated by warm rain, which is initiated just above the cloud base by nucleation of larger sea spray particles (Rosenfeld et al. 2012; Shpund et al. 2019) and subsequent collision–coalescence process. Melting ice hydrometeors formed at upper levels add to the rainfall but do not dominate it.

In this conceptual model (Fig. 13), the external rainbands (Figs. 13b,c) outside the main circulation of the hurricane have much weaker surface wind speeds that raise relatively fewer sea spray aerosols compared with inner eyewall regions. Hypothetically, large concentrations of UAPs may still come from sources such as anthropogenic air pollution, including possibly the oil rigs in the Gulf of Mexico (Kumar et al. 2014). An illustration of the microphysical composition of the hurricane external rainbands under high and low UAP concentration scenarios is presented in Figs. 13b and 13c, respectively. In general, the outer rainbands region has much smaller vertical wind shear, which favors convection development. For the high-UAP scenario (Fig. 13b), according to Fan et al. (2018), the activation of UAPs above cloud base in clouds with heavy warm

rain can enhance condensational heating that invigorates the convection. Stronger vertical motion also facilitates condensation aloft, along with increased upward transport of liquid water content and hydrometeors, which stimulates mixed-phase hydrometeor formation. The latent heat release arising from liquid to ice transition further enhances convection (Rosenfeld et al. 2008). The enhanced ice-phase formation includes not only ice crystals but also hail and graupel (Rosenfeld et al. 2008). Collisions between hail/graupel and ice crystals due to the differences in their terminal velocities within a supercooled water environment can lead to charge separation and lightning discharges (Williams 1989). Falling hail/graupel below the ML melts into raindrops and further enhances surface precipitation intensity.

In this conceptual model, the low-UAP scenario (Fig. 13c) of external rainband clouds implies less vertical development due to the lack of condensational heating with decreased UAP concentration. The cloud tops are lower with no obvious overshooting tops and weaker anvil clouds. The precipitation type is determined by both warm-rain and mixed-phase precipitation processes. The source of raindrops can be either from coalescence of cloud droplets or melted ice particles aloft. Since the vertical motion is weaker in the low-UAP scenario, hail/graupel seldom forms because of the lack of water content and ice crystals. Less lightning activity is expected under the low-UAP scenario. A more comprehensive study is needed to verify the validity of the suggested conceptual model.

5. Conclusions

In this study, we investigated differing cloud microphysical structures of the eyewall and the external rainbands of two hurricanes. Based on the results of our analysis, the microphysical variability is likely caused by the differences in the strength of the vertical wind shear between the eyewall and the external rainbands. The updrafts in the eyewall clouds are sheared and rarely overshoot above the cloud canopy, while the external rainband clouds are organized with much weaker vertical wind shear that favors development of deep updraft cores that regularly overshoot above the cloud canopy. Added aerosols, either from sea spray or air pollution, are hypothesized to be the invigoration sources of convection.

The *GOES-16* provides new insights into the identification of convective vigor affecting the structure of cloud tops. Relatively smooth tops of the eyewall clouds indicate weaker convection, mostly organized by the hurricane-scale winds. The “boiling” appearance of the cloud tops of the external rainbands reveals its highly convective vigor. In this study, we analyzed the cloud-top 10.4- μm brightness temperatures of Hurricanes Harvey and Florence and found that the strongest overshooting tops at the external rainbands are colder than eyewall cloud tops. The multichannel microphysical RGB scheme shows more detailed information about the cloud-top microstructure. The bright yellow in this study is a combination of thick cloud optical depth ($r0.86$; high red), high concentration of small ice crystals ($r1.6$; high green), and cold cloud top ($T10.4$; low blue). It is handy to distinguish the state of convective clouds life cycle by combining multichannel RGB with cloud-top smoothness. This scheme has broad application potential for further studies in various types of cloud systems.

The radar CVPs provide detailed representation of the time–height structure of the storm to support the proposed conceptual model. This is based on the ability of dual-polarization radars to retrieve the hydrometeor phase, concentration, and sizes. The eyewall precipitation is dominated by tropical warm rain that is formed mostly below the ML. The ice-phase hydrometeors in the eyewall region are dominated by high concentration of small ice crystals. The external rainband clouds are highly convective as denoted by relatively high Z (exceeding 20 dBZ) above the ML and less pronounced depression of ρ_{hv} in the ML. The enhanced mixed-phase processes aloft are indicative of strong updrafts, which lead to heavy precipitation that mostly originates from the mixed-phase zone marked by intense lightning activity. This extremely heavy rain from the external cloud

bands caused most of the flooding in both Harvey and Florence.

In this paper, we combined ground-based radar measurements with satellite observations to study hurricane microphysical structure from surface to cloud top. This fills the gap between observational techniques, shows good consistency between the two analyses, and provides new insights in understanding the significantly different cloud microphysical and dynamical structures in hurricane eyewall and external rainband. The proposed conceptual model outlines the cloud microphysics we understand to date, emphasizes possible role of UAPs, and motivates the need for further direct measurements of UAP.

Acknowledgments. Funding was provided by NOAA/Office of Oceanic and Atmospheric Research under NOAA–University of Oklahoma Cooperative Agreement NA16OAR4320115, U.S. Department of Commerce, and by the U.S. National Weather Service, Federal Aviation Administration, and U.S. Department of Defense program for modernization of NEXRAD. Additional funding came from the U.S. Department of Energy Grants DE-SC0014295 and DE-SC0018967. Data availability statement: Data used here were obtained from the National Centers for Environmental Information.

REFERENCES

- Ávila, E. E., R. E. Burgesser, N. E. Castellano, A. B. Collier, R. H. Compagnucci, and A. R. W. Hughes, 2010: Correlations between deep convection and lightning activity on a global scale. *J. Atmos. Sol.-Terr. Phys.*, **72**, 1114–1121, <https://doi.org/10.1016/j.jastp.2010.07.019>.
- Benjamin, S. G., and Coauthors, 2016: A North American hourly assimilation and model forecast cycle: The Rapid Refresh. *Mon. Wea. Rev.*, **144**, 1669–1694, <https://doi.org/10.1175/MWR-D-15-0242.1>.
- Blake, S. E., and A. D. Zelinsky, 2018: National Hurricane Center Tropical Cyclone Report: Hurricane Harvey. NOAA/NWS Rep. AL092017, 76 pp., https://www.nhc.noaa.gov/data/tcr/AL092017_Harvey.pdf.
- Brown, B. R., M. M. Bell, and A. J. Frambach, 2016: Validation of simulated hurricane drop size distributions using polarimetric radar. *Geophys. Res. Lett.*, **43**, 910–917, <https://doi.org/10.1002/2015GL067278>.
- Bukovič, P., D. Zrnić, and G. F. Zhang, 2017: Winter precipitation liquid–ice phase transitions revealed with polarimetric radar and 2DVD observations in central Oklahoma. *J. Appl. Meteor. Climatol.*, **56**, 1345–1363, <https://doi.org/10.1175/JAMC-D-16-0239.1>.
- , A. Ryzhkov, D. Zrnić, and G. F. Zhang, 2018: Polarimetric radar relations for quantification of snow based on disdrometer data. *J. Appl. Meteor. Climatol.*, **57**, 103–120, <https://doi.org/10.1175/JAMC-D-17-0090.1>.
- Chang, W. Y., T. C. C. Wang, and P. L. Lin, 2009: Characteristics of the raindrop size distribution and drop shape relation in

- typhoon systems in the western Pacific from the 2D video disdrometer and NCU C-band polarimetric radar. *J. Atmos. Oceanic Technol.*, **26**, 1973–1993, <https://doi.org/10.1175/2009JTECHA1236.1>.
- , W. C. Lee, and Y. C. Liou, 2015: The kinematic and microphysical characteristics and associated precipitation efficiency of subtropical convection during SoWMEX/TiMREX. *Mon. Wea. Rev.*, **143**, 317–340, <https://doi.org/10.1175/MWR-D-14-00081.1>.
- Chen, B. J., Y. Wang, and J. Ming, 2012: Microphysical characteristics of the raindrop size distribution in Typhoon Morakot (2009). *J. Trop. Meteorol.*, **18**, 162–171, <https://doi.org/10.3969/j.issn.1006-8775.2012.02.006>.
- Cullen, M., 2013: The Houston Lightning Mapping Array: Network installation and preliminary analysis. M.S. thesis, Dept. of Atmospheric Sciences, Texas A&M University, 74 pp.
- Czajkowski, J., and J. Done, 2014: As the wind blows? Understanding hurricane damages at the local level through a case study analysis. *Wea. Climate Soc.*, **6**, 202–217, <https://doi.org/10.1175/WCAS-D-13-00024.1>.
- Dai, J., X. Yu, D. Rosenfeld, and X. H. Xu, 2007: Microphysical effects of cloud seeding in supercooled stratiform clouds observed from NOAA satellite. *Acta Meteor. Sin.*, **21**, 224–233.
- Dawson, D. T., E. R. Mansell, and M. R. Kumjian, 2015: Does wind shear cause hydrometeor size sorting? *J. Atmos. Sci.*, **72**, 340–348, <https://doi.org/10.1175/JAS-D-14-0084.1>.
- Didlake, A. C., and M. R. Kumjian, 2017: Examining polarimetric radar observations of bulk microphysical structures and their relation to vortex kinematics in Hurricane Arthur (2014). *Mon. Wea. Rev.*, **145**, 4521–4541, <https://doi.org/10.1175/MWR-D-17-0035.1>.
- , and —, 2018: Examining storm asymmetries in Hurricane Irma (2017) using polarimetric radar observations. *Geophys. Res. Lett.*, **45**, 13 513–13 522, <https://doi.org/10.1029/2018GL080739>.
- Fan, J., and Coauthors, 2009: Dominant role by vertical wind shear in regulating aerosol effects on deep convective clouds. *J. Geophys. Res.*, **114**, D22206, <https://doi.org/10.1029/2009JD012352>.
- , and Coauthors, 2018: Substantial convection and precipitation enhancements by ultrafine aerosol particles. *Science*, **359**, 411–418, <https://doi.org/10.1126/science.aan8461>.
- Feng, Y. C., and M. M. Bell, 2019: Microphysical characteristics of an asymmetric eyewall in major Hurricane Harvey (2017). *Geophys. Res. Lett.*, **46**, 461–471, <https://doi.org/10.1029/2018GL080770>.
- Gadelmawla, E. S., M. M. Koura, T. M. A. Maksoud, I. M. Elewa, and H. H. Soliman, 2002: Roughness parameters. *J. Mater. Process. Technol.*, **123**, 133–145, [https://doi.org/10.1016/S0924-0136\(02\)00060-2](https://doi.org/10.1016/S0924-0136(02)00060-2).
- Goren, T., and D. Rosenfeld, 2012: Satellite observations of ship emission induced transitions from broken to closed cell marine stratocumulus over large areas. *J. Geophys. Res.*, **117**, D17206, <https://doi.org/10.1029/2012JD017981>.
- Griffin, E. M., T. J. Schuur, and A. V. Ryzhkov, 2018: A polarimetric analysis of ice microphysical processes in snow, using quasi-vertical profiles. *J. Appl. Meteor. Climatol.*, **57**, 31–50, <https://doi.org/10.1175/JAMC-D-17-0033.1>.
- Iacovelli, D., 1999: The Saffir/Simpson Hurricane Scale: An interview with Dr. Robert Simpson. *Mariners Weather Log*, Vol. 43, National Weather Service, NOAA, Silver Spring, MD, 10–12, <https://vos.noaa.gov/MWL/apr1999.pdf>.
- Iltoviz, E., A. P. Khain, N. Benmoshe, V. T. J. Phillips, and A. V. Ryzhkov, 2016: Effect of aerosols on freezing drops, hail, and precipitation in a midlatitude storm. *J. Atmos. Sci.*, **73**, 109–144, <https://doi.org/10.1175/JAS-D-14-0155.1>.
- Justice, C. O., J. R. G. Townshend, E. F. Vermote, E. Masuoka, R. E. Wolfe, N. Saleous, D. P. Roy, and J. T. Morisette, 2002: An overview of MODIS Land data processing and product status. *Remote Sens. Environ.*, **83**, 3–15, [https://doi.org/10.1016/S0034-4257\(02\)00084-6](https://doi.org/10.1016/S0034-4257(02)00084-6).
- Khain, A. P., V. Phillips, N. Benmoshe, and A. Pokrovsky, 2012: The role of small soluble aerosols in the microphysics of deep maritime clouds. *J. Atmos. Sci.*, **69**, 2787–2807, <https://doi.org/10.1175/2011JAS3649.1>.
- Kumar, P., and Coauthors, 2014: Ultrafine particles in cities. *Environ. Int.*, **66**, 1–10, <https://doi.org/10.1016/j.envint.2014.01.013>.
- Kumjian, M. R., and A. V. Ryzhkov, 2012: The impact of size sorting on the polarimetric radar variables. *J. Atmos. Sci.*, **69**, 2042–2060, <https://doi.org/10.1175/JAS-D-11-0125.1>.
- Lensky, I. M., and D. Rosenfeld, 2006: The time-space exchangeability of satellite retrieved relations between cloud top temperature and particle effective radius. *Atmos. Chem. Phys.*, **6**, 2887–2894, <https://doi.org/10.5194/acp-6-2887-2006>.
- , and —, 2008: Clouds-Aerosols-Precipitation Satellite Analysis Tool (CAPSAT). *Atmos. Chem. Phys.*, **8**, 6739–6753, <https://doi.org/10.5194/acp-8-6739-2008>.
- May, P. T., J. D. Kepert, and T. D. Keenan, 2008: Polarimetric radar observations of the persistently asymmetric structure of Tropical Cyclone Ingrid. *Mon. Wea. Rev.*, **136**, 616–630, <https://doi.org/10.1175/2007MWR2077.1>.
- Murphy, A., 2018: A microphysical analysis of the stratiform rain region of mesoscale convective systems using polarimetric radar and in situ aircraft measurements. M.S. thesis, Dept. of Meteorology, University of Oklahoma, 155 pp.
- NOAA, 2018: How many direct hits by hurricanes of various categories have affected each state? Frequently Asked Questions about Hurricanes, NHC, <http://www.aoml.noaa.gov/hrd/tcfaq/E19.html>.
- Peckham, S. E., T. G. Smirnova, S. G. Benjamin, J. M. Brown, and J. S. Kenyon, 2016: Implementation of a digital filter initialization in the WRF model and its application in the Rapid Refresh. *Mon. Wea. Rev.*, **144**, 99–106, <https://doi.org/10.1175/MWR-D-15-0219.1>.
- Pinsky, M., and A. Khain, 2018: Theoretical analysis of the entrainment-mixing process at cloud boundaries. Part I: Droplet size distributions and humidity within the interface zone. *J. Atmos. Sci.*, **75**, 2049–2064, <https://doi.org/10.1175/JAS-D-17-0308.1>.
- Proctor, F., and G. Switzer, 2016: Numerical simulation of HIWC conditions with the terminal area simulation system. *Eighth AIAA Atmospheric and Space Environments Conf.*, Washington, DC, American Institute of Aeronautics and Astronautics, <https://doi.org/10.2514/6.2016-4203>.
- Rasmussen, K. L., M. D. Zuluaga, and R. A. Houze, 2014: Severe convection and lightning in subtropical South America. *Geophys. Res. Lett.*, **41**, 7359–7366, <https://doi.org/10.1002/2014GL061767>.
- Rosenfeld, D., 2018: Cloud-aerosol-precipitation interactions based of satellite retrieved vertical profiles of cloud microstructure. *Remote Sensing of Aerosols, Clouds, and Precipitation*, T. Islam et al., Eds., Elsevier, 129–152.
- , and I. M. Lensky, 1998: Satellite-based insights into precipitation formation processes in continental and maritime convective clouds. *Bull. Amer. Meteor. Soc.*, **79**, 2457–2476, [https://doi.org/10.1175/1520-0477\(1998\)079<2457:SBIHPF>2.0.CO;2](https://doi.org/10.1175/1520-0477(1998)079<2457:SBIHPF>2.0.CO;2).

- , W. L. Woodley, A. Lerner, G. Kelman, and D. T. Lindsey, 2008: Satellite detection of severe convective storms by their retrieved vertical profiles of cloud particle effective radius and thermodynamic phase. *J. Geophys. Res.*, **113**, D04208, <https://doi.org/10.1029/2007JD008600>.
- , —, A. Khain, W. R. Cotton, G. Carrio, I. Ginis, and J. H. Golden, 2012: Aerosol effects on microstructure and intensity of tropical cyclones. *Bull. Amer. Meteor. Soc.*, **93**, 987–1001, <https://doi.org/10.1175/BAMS-D-11-00147.1>.
- , G. Liu, X. Yu, Y. Zhu, J. Dai, X. Xu, and Z. Yue, 2014: High-resolution (375 m) cloud microstructure as seen from the NPP/VIIRS satellite imager. *Atmos. Chem. Phys.*, **14**, 2479–2496, <https://doi.org/10.5194/acp-14-2479-2014>.
- , and Coauthors, 2016: Satellite retrieval of cloud condensation nuclei concentrations by using clouds as CCN chambers. *Proc. Natl. Acad. Sci. USA*, **113**, 5828–5834, <https://doi.org/10.1073/pnas.1514044113>.
- Rudlosky, S. D., S. J. Goodman, K. S. Virts, and E. C. Bruning, 2019: Initial geostationary lightning mapper observations. *Geophys. Res. Lett.*, **46**, 1097–1104, <https://doi.org/10.1029/2018GL081052>.
- Ryzhkov, A., and D. Zrnić, 2019: *Radar Polarimetry for Weather Observations*. Springer International, 486 pp.
- , S. E. Giangrande, and T. J. Schuur, 2005: Rainfall estimation with a polarimetric prototype of WSR-88D. *J. Appl. Meteor.*, **44**, 502–515, <https://doi.org/10.1175/JAM2213.1>.
- , P. F. Zhang, H. Reeves, M. Kumjian, T. Tschallener, S. Tromel, and C. Simmer, 2016: Quasi-vertical profiles—A new way to look at polarimetric radar data. *J. Atmos. Oceanic Technol.*, **33**, 551–562, <https://doi.org/10.1175/JTECH-D-15-0020.1>.
- Shpund, J., A. Khain, and D. Rosenfeld, 2019: Effects of sea spray on the dynamics and microphysics of an idealized tropical cyclone. *J. Atmos. Sci.*, **76**, 2213–2234, <https://doi.org/10.1175/JAS-D-18-0270.1>.
- Stewart, S., and R. Berg, 2019: National Hurricane Center Tropical Cyclone Report: Hurricane Florence. NOAA/NWS Rep. AL062018, 98 pp., https://www.nhc.noaa.gov/data/tcr/AL062018_Florence.pdf.
- Tobin, D. M., and M. R. Kumjian, 2017: Polarimetric radar and surface-based precipitation-type observations of ice pellet to freezing rain transitions. *Wea. Forecasting*, **32**, 2065–2082, <https://doi.org/10.1175/WAF-D-17-0054.1>.
- Tokay, A., P. G. Bashor, E. Habib, and T. Kasparis, 2008: Raindrop size distribution measurements in tropical cyclones. *Mon. Wea. Rev.*, **136**, 1669–1685, <https://doi.org/10.1175/2007MWR2122.1>.
- Tourville, N., G. Stephens, M. DeMaria, and D. Vane, 2015: Remote sensing of tropical cyclones: Observations from CloudSat and A-Train profilers. *Bull. Amer. Meteor. Soc.*, **96**, 609–622, <https://doi.org/10.1175/BAMS-D-13-00282.1>.
- Ulbrich, C. W., and L. G. Lee, 2002: Rainfall characteristics associated with the remnants of Tropical Storm Helene in upstate South Carolina. *Wea. Forecasting*, **17**, 1257–1267, [https://doi.org/10.1175/1520-0434\(2002\)017<1257:RCAWTR>2.0.CO;2](https://doi.org/10.1175/1520-0434(2002)017<1257:RCAWTR>2.0.CO;2).
- Wang, M. J., K. Zhao, M. Xue, G. F. Zhang, S. Liu, L. Wen, and G. Chen, 2016: Precipitation microphysics characteristics of a Typhoon Matmo (2014) rainband after landfall over eastern China based on polarimetric radar observations. *J. Geophys. Res. Atmos.*, **121**, 12 415–12 433, <https://doi.org/10.1002/2016JD025307>.
- Williams, E. R., 1989: The tripole structure of thunderstorms. *J. Geophys. Res.*, **94**, 13 151–13 167, <https://doi.org/10.1029/JD094iD11p13151>.
- Wilson, J. W., and D. M. Pollock, 1974: Rainfall measurements during Hurricane Agnes by 3 overlapping radars. *J. Appl. Meteor.*, **13**, 835–844, [https://doi.org/10.1175/1520-0450\(1974\)013<0835:RMDHAB>2.0.CO;2](https://doi.org/10.1175/1520-0450(1974)013<0835:RMDHAB>2.0.CO;2).
- Wu, D., and Coauthors, 2018: Kinematics and microphysics of convection in the outer rainband of Typhoon Nida (2016) revealed by polarimetric radar. *Mon. Wea. Rev.*, **146**, 2147–2159, <https://doi.org/10.1175/MWR-D-17-0320.1>.
- Wu, S. N., and B. J. Soden, 2017: Signatures of tropical cyclone intensification in satellite measurements of ice and liquid water content. *Mon. Wea. Rev.*, **145**, 4081–4091, <https://doi.org/10.1175/MWR-D-17-0046.1>.
- Xu, W. X., S. A. Rutledge, and W. J. Zhang, 2017: Relationships between total lightning, deep convection, and tropical cyclone intensity change. *J. Geophys. Res. Atmos.*, **122**, 7047–7063, <https://doi.org/10.1002/2017JD027072>.
- Yu, C. K., and C. L. Tsai, 2013: Structural and surface features of arc-shaped radar echoes along an outer tropical cyclone rainband. *J. Atmos. Sci.*, **70**, 56–72, <https://doi.org/10.1175/JAS-D-12-090.1>.
- Zhang, J., and Coauthors, 2016: Multi-Radar Multi-Sensor (MRMS) quantitative precipitation estimation: Initial operating capabilities. *Bull. Amer. Meteor. Soc.*, **97**, 621–638, <https://doi.org/10.1175/BAMS-D-14-00174.1>.
- Zhang, W., G. Villarini, G. A. Vecchi, and J. A. Smith, 2018: Urbanization exacerbated the rainfall and flooding caused by Hurricane Harvey in Houston. *Nature*, **563**, 384–388, <https://doi.org/10.1038/s41586-018-0676-z>.
- Zheng, Y. T., and D. Rosenfeld, 2015: Linear relation between convective cloud base height and updrafts and application to satellite retrievals. *Geophys. Res. Lett.*, **42**, 6485–6491, <https://doi.org/10.1002/2015GL064809>.
- Zhu, Y. N., D. Rosenfeld, X. Yu, G. H. Liu, J. Dai, and X. H. Xu, 2014: Satellite retrieval of convective cloud base temperature based on the NPP/VIIRS Imager. *Geophys. Res. Lett.*, **41**, 1308–1313, <https://doi.org/10.1002/2013GL058970>.